Image formation, resolution, and height measurement in scanning ion conductance microscopy

Johannes Rheinlaender and Tilman E. Schäffer[a)]
Institute of Applied Physics, University of Erlangen-Nuremberg, Staudtstr. 7, Bldg. A3, 91058 Erlangen, Germany

(Received 30 December 2008; accepted 23 March 2009; published online 7 May 2009)

Scanning ion conductance microscopy (SICM) is an emerging tool for the noncontact investigation of biological samples such as live cells. It uses an ion current through the opening of a tapered nanopipette filled with an electrolyte for topography measurements. Despite its successful application to numerous systems no systematic investigation of the image formation process has yet been performed. Here, we use finite element modeling to investigate how the scanning ion conductance microscope images small particles on a planar surface, providing a fundamental characterization of the imaging process. We find that a small particle appears with a height that is only a fraction of its actual height. This has significant consequences for the quantitative interpretation of SICM images. Furthermore, small and low particles are imaged as rings in certain cases. This can cause small, closely spaced particles to appear with a lateral orientation that is rotated by 90°. Considering both real space and spatial frequency space we find that a reasonable and useful definition of lateral resolution of SICM is the smallest distance at which two small particles can clearly be resolved from each other in an image. We find that this resolution is approximately equal to three times the inner radius of the pipette tip opening. © *2009 American Institute of Physics*. [DOI: 10.1063/1.3122007]

I. INTRODUCTION

Scanning ion conductance microscopy (SICM), introduced in 1989 by Hansma *et al.*[1] and further developed by Korchev *et al.*,[2] allows investigating sample topography without mechanical contact. In a scanning ion conductance microscope, an ion current through an electrolyte-filled nanopipette is induced by a voltage that is applied between one electrode inside and another one outside the pipette [Fig. 1(a)]. The current decreases when the pipette approaches the sample, thereby providing a measure of the pipette-sample distance. Using the ion current as an input to a feedback loop controlling the vertical pipette position, this allows imaging the sample topography by laterally scanning the pipette. SICM has been applied to a wide variety of biophysical systems such as proteins on cell membranes,[3] long-term dynamics[4] and chemical activity[5] of live cells, and suspended artificial membranes.[6] By combination with other microscopy techniques, additional sample properties such as fluorescence[7] or porosity[8] can be recorded. Recent work by Sánchez *et al.*[9] reports the measurement of mechanical sample properties with the scanning ion conductance microscope.

The resolution in SICM is mainly determined by the size of the pipette tip opening. However, a systematic investigation of the factors affecting lateral resolution has not yet been performed. Hansma *et al.*[1] used a macroscopic pipette and sample to evaluate the resolution, but this method does not allow the lateral resolution to be derived due to the perfect periodicity of their sample. Korchev *et al.*[2] assumed a virtual spherical tip of the same radius as the inner pipette tip opening. Nitz *et al.*[10] introduced a mathematical model that results in a rough estimation of the current-distance dependence of the ion current for planar samples. They also assessed the influence of ion current noise on lateral position measurements, but did not consider the finite lateral resolution itself. Adenle and Fitzgerald[11] applied a state-space model to obtain the distribution of the ion current density, but they did not take into account the effect of the pipette-sample distance on the ion current density. Shevchuk *et al.*[3] succeeded in imaging single proteins on the membrane of a living cell using quartz pipettes.

In this paper we investigate the image formation and resolution in SICM using finite element modeling (FEM). First, we describe the influence of the pipette-sample distance on the ion current for a planar sample. Both the total measured current and the current density distribution change dramatically when approaching the sample. This has a huge impact on the SICM imaging process, which we characterize by calculating images of small particles on a planar surface. The images depend significantly on particle height and pipette-sample distance.

There are different possible definitions of resolution. In this paper we use a reasonable and useful definition of resolution, which is directly accessible in scanning probe microscopy: the smallest distance at which two individual particles on a planar surface can clearly be resolved from each other in an image. We show that the lateral resolution defined in this way is approximately equal to three times the inner radius of the pipette tip opening. We also discuss an alternative definition of resolution in spatial frequency space using the contrast transfer function (CTF), giving the same result.

[a)]Electronic mail: schaeffer@physik.uni-erlangen.de. Tel.: +49 (9131) 85-28431. FAX: +49 (9131) 85-28423.

II. MODELING

The flow of the ionic current through the electrolyte can be broken down into three regions [Fig. 1(a)]: (1) from the pipette electrode to the pipette tip region, (2) through the tip region [=region in the vicinity of the pipette tip, indicated by the red box in Fig. 1(a)], and (3) from the tip region to the bath electrode. The electrical "pipette resistance" of region 1 can be calculated analytically[12] when modeling the pipette as a hollow cone

$$R_p = \frac{1}{\sigma} \frac{1}{\pi r_u \tan \alpha}. \quad (1)$$

σ is the conductivity of the electrolyte, r_u is the cone opening radius at the transition to the pipette tip region, and α is the cone angle of the pipette (we used $\alpha = 3°$ except where noted otherwise). R_p is independent of the conditions in the pipette tip region. The resistance of region 3 is much smaller than R_p for typical SICM pipettes and can thus be neglected. To determine the "tip resistance" of region 2, R_t, we used FEM (COMSOL MULTIPHYSICS V3.3: electromagnetics module/conductive media DC, COMSOL AB, Stockholm, Sweden). The geometry of the model is shown in Figs. 1(b) and 1(c). We assumed the pipette tip opening to be exactly planar, horizontally oriented, and with sharp edges, corresponding well with electron microscopy data. The pipette is then described completely by the inner opening radius r_i, the outer opening radius r_o (here $r_o = 2r_i$), and the pipette cone angle α. The ratio r_i/r_o and the cone angle are assumed to be constant in the lower part of the pipette.[13] On the bottom the electrolyte is bounded by the sample, modeled here as a planar, horizontal surface with two cylindrical particles of radius r and height h_0. All boundaries are insulating, except the disk-shaped areas inside and outside the pipette [red and blue areas in Figs. 1(b) and 1(c), respectively]. The size of the model boundary box was between 14 and $20r_i$ in lateral x- and y-direction and about $4r_i$ in vertical z-direction. The FEM mesh was refined once, consisting of typically 26 000 tetrahedral elements and 39 000 degrees of freedom (duration to solve ≈ 10 s on a current workstation). The total electrical resistance of the circuit, R, can then be described by summing the pipette resistance and the tip resistance,

$$R = R_p + R_t. \quad (2)$$

The measured electrical current is obtained by

$$I = \frac{U}{R} = \frac{U}{R_p + R_t}, \quad (3)$$

where U is the voltage applied between the electrodes. We neglected the resistances in the wires and in the electrodes.

In an experiment the z-position of the pipette is usually controlled by a feedback loop during x-y-scanning to keep the current constant. To calculate such a topography image, $z(x,y)$, at a constant current, is computationally intensive, because for every x-y-position the z-position needs to be varied to find the position with that current. We found, however, that the effect of small topographic objects on the current-distance curve, $I(z_0)$, is mainly a small shift of the curve along the z_0-axis, with the shape of the curve unchanged. z_0 is the pipette-sample distance with respect to the planar sample surface. Therefore, in order to reduce the computation time, we initially calculate a current image $I(x,y)$ at a constant vertical pipette position, z_0. With the knowledge of $I(z_0)$ we then convert this current image into a topography image, $z(x,y)$, at a constant current.

III. RESULTS AND DISCUSSION

A. Ion current density in the pipette tip region

Figure 2 shows the calculated ion current density in the vicinity of the pipette tip opening above a planar, insulating sample. Inside the pipette the current density is relatively high, increases at the inner edges of the opening, and drops quickly on the outside. When the pipette is far away from the sample [Fig. 2(a)], the far field of the current density is radially symmetric on the first order (semicircular contour lines). This behavior is changed by the presence of a sample. Due to symmetry, the current density directly above the (insulating) sample, vertically below the center of the opening, is always zero. Therefore, the current density above the sample is slightly larger below the pipette walls than it is below the pipette center even for large pipette-sample distances [Fig. 2(b)]. This effect is amplified for smaller pipette-sample distances [Figs. 2(c) and 2(d)], because then the current density is increased in the narrowing gap between the

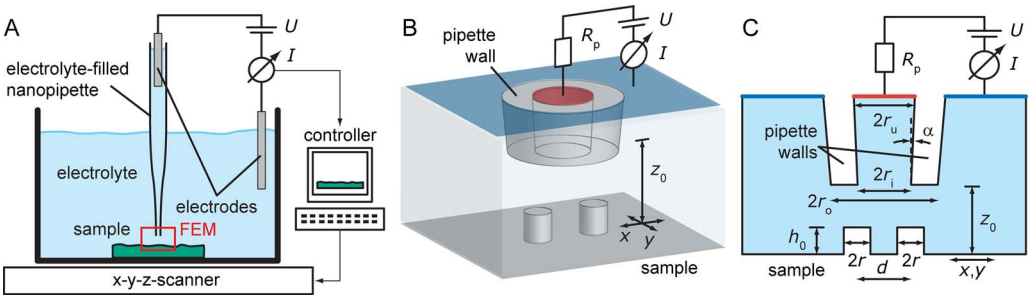

FIG. 1. (Color online) (a) Schematic of a SICM setup, which is based on an electrolyte-filled nanopipette. The ion current, I, induced by an applied voltage between the two electrodes, U, is measured by a nanoampere amplifier and used for feedback via a computer-based controller and an x-y-z-scanner. (b) Three-dimensional schematic and (c) two-dimensional cross section of the pipette tip region that are modeled with finite element analysis, indicated by a red box in (a), here shown for a planar sample with two cylindrical particles (radius r, height h_0, and distance d). The scanning process is simulated by changing the relative pipette-sample orientation (x,y,z_0). A series resistance R_p suffices to model the remaining upper part of the pipette.

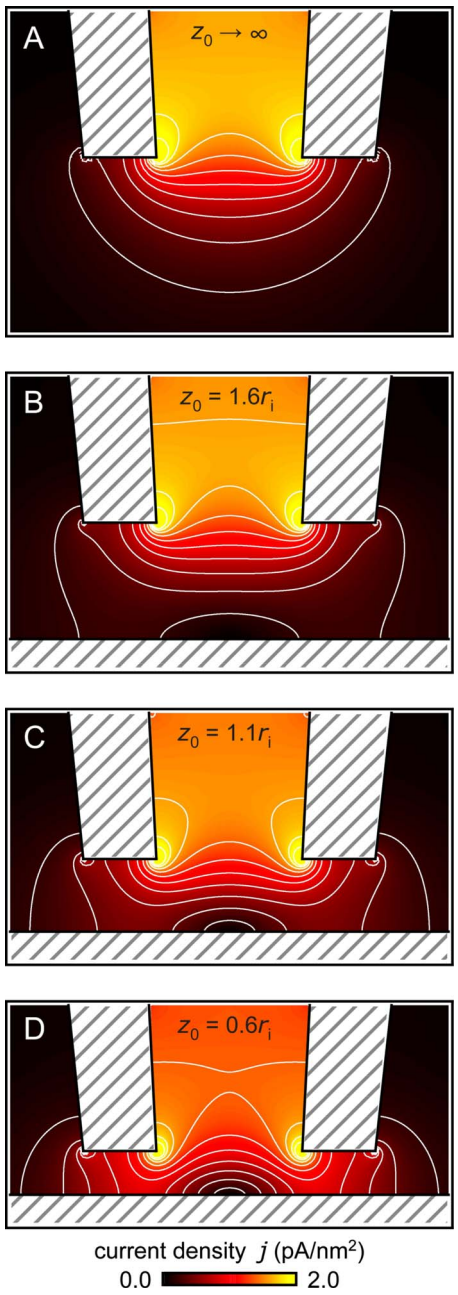

FIG. 2. (Color online) Cross section through the pipette showing the calculated distribution of the ion current density in the tip region. (a) When the pipette-sample distance is much larger than the inner pipette radius ($z_0 \gg r_i$), the current density below the tip has approximately spherical isosurfaces (white lines: equally spaced contour lines at $0.2, 0.4, \ldots, 2.0$ pA/nm^2). (b) When the tip comes into the vicinity of a planar sample ($z_0=1.6r_i$), these isosurfaces start deforming. [(c) and (d)] At even smaller pipette-sample distances ($z_0=1.1r_i$ and $z_0=0.6r_i$, respectively), a ring-shaped area of high current density is formed below the pipette walls. Parameters used for this figure: inner pipette radius $r_i=25$ nm, outer pipette radius $r_o=2r_i$, conductivity $\sigma=1$ S m^{-1}, and applied voltage $U=1$ V.

pipette walls and the sample ("current squeezing"). Additionally, the current density inside the pipette decreases for decreasing pipette-sample distance, because of the increasing resistance of the tip region.

We note that the strong distortion of the current density contour lines due to the presence of the planar sample, even at a fairly large pipette-sample distance ($z_0=1.6\ r_i$), does not support the notion of the pipette generally acting as a "virtual spherical sensor" as introduced previously.[2]

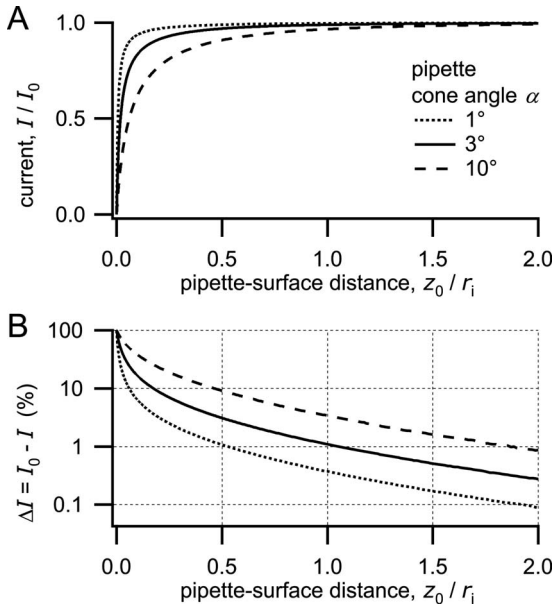

FIG. 3. (a) Ion current through the pipette, I, in units of saturation current, I_0, as a function of pipette-sample distance, z_0, in units of the inner pipette radius r_i, obtained by a series of FEM calculations on a planar sample. (b) Corresponding ion current drop, $\Delta I=I_0-I$. This ion current drop is used in SICM experiments to set the pipette-sample distance, z_0.

B. Current-distance behavior on a planar surface

To determine the dependence of the ion current on the pipette-sample distance, z_0, above a planar sample [Fig. 1(c) for $h_0=0$], we calculated the current through the pipette as a function of z_0 for three different values of the pipette cone angle α [Fig. 3(a)]. The current is maximum at a saturation current I_0 for large z_0 and sharply decreases to zero for $z_0 \rightarrow 0$. Interestingly, this sharp current drop occurs at pipette-sample distances significantly smaller than the length scale that is given by the inner opening radius of the pipette. For example, 90% of the current drop occurs within a distance of only $0.2r_i$ (for $\alpha=3°$). A larger cone angle results in a larger current drop distance. The current drop distance is also affected by the ratio of the outer to inner radius, r_o/r_i (here, $r_o/r_i=2$), but the influence is in the subpercentage range for typical large values of z_0 (data not shown). The current drop $\Delta I=I_0-I$ correspondingly increases for decreasing pipette-sample distance [Fig. 3(b)]. For example, for a pipette with $\alpha=3°$, the current drop is 1% of I_0, when the pipette is one radius away from the sample ($z_0=r_i$). Table I shows the saturation current and the corresponding electrical resistance for three values of α.

TABLE I. Values for saturation current, I_0, and total resistance, $R=U/I_0$, for typical pipette cone angles α. For example, $I_0=1.58$ nA and $R=63.1$ MΩ for $\alpha=3°$, $r_i=100$ nm, $\sigma=1$ S/m, and $U=100$ mV.

Pipette cone angle, α (deg)	Saturation current, $I_0/(r_i\sigma U)$ [nA/(nm S m^{-1} V)]	Total resistance, $R\times(r_i\sigma)$ (GΩ nm S m)
1	0.0541	16.2
3	0.158	6.31
10	0.487	2.05

During imaging, a feedback loop adjusts the position of the z-scanner to keep the current drop ΔI at a given setpoint value. A large current drop results in a small pipette-sample distance, and vice versa. We note that in recent experimental setups the vertical pipette position is often modulated sinusoidally.[14,15] For large modulation amplitudes the current then oscillates between I_0 and I, so the peak-to-peak amplitude of the current signal is equal to ΔI.

C. Single particle on a planar surface

As a basic step for characterizing the SICM imaging process, we first focus on the imaging of a single particle in form of a thin vertical cylinder with a radius of $r=r_i/2$ on a planar sample. As we will see, the particle height has a significant influence on the resulting image. To demonstrate the different effects, we calculated topography (constant current) images for different pipette-sample distances and for two different particle heights, $h_0=r_i$ ["high particle", Figs. 4(a) and 4(b)] and $h_0=r_i/2$ ["low particle", Figs. 4(c)–4(e)], respectively. The chosen pipette-sample distances correspond to typical experimental values.

From Fig. 4(a) and its cross section in Fig. 4(a)' it can be seen that the large particle, scanned at a large pipette-sample distance, $z_0=1.6r_i$, is imaged with a bell-shaped topography profile of FWHM$=3.2r_i$ and height $0.16h_0$. The particle therefore appears laterally smeared out to a width of about three times the inner pipette radius and appears vertically compressed to only 16% of its actual height. For comparison, the outline of the pipette tip opening is shown as dotted circles in Fig. 4(a). When the pipette-sample distance is reduced [Figs. 4(b) and 4(b)'], the image of the particle appears at about the same width, but at a significant larger height ($0.25h_0$). Furthermore, a dip is developed in its center, resulting in a ring-shaped image. Even though the pipette almost touches the particle, the particle still appears at a height that is only a quarter of the actual height.

The low particle, on the other hand, appears with a dip even for the large pipette-sample distance [Figs. 4(c) and 4(c)']. Its apparent height, $0.06h_0$, is even smaller and the profile is wider, FWHM$=5r_i$, than in the corresponding case of the high particle [Fig. 4(a)']. When the pipette-sample distance is reduced [Figs. 4(d) and 4(d)'], the apparent height increases to $0.10h_0$ and the dip becomes more pronounced. This trend continues for even smaller distances [Figs. 4(e) and 4(e)'].

Figure 4(f) shows the full width at half maximum (FWHM) values from the particles in Figs. 4(a)–4(e) for the different pipette-sample distances and particle heights. As it can be seen the FWHM value is reduced (so the image becomes "sharper") for larger particle heights and for smaller pipette-sample distances.

These differences in particle appearance can be explained by considering the distribution of the ion current in the tip region. The presence of a small object in the tip region causes a current drop that is proportional to the value of the current density at the regarding object position. In other words, the small particle images the ion current density distribution in the tip region (Fig. 2). In the case of a large pipette-sample distance [Fig. 2(b)], the distribution of the current density at half height between pipette and sample, to where the high particle extends to, is maximum in the center and decreases for larger distances. This results in the bell shape of the image of a high particle [Fig. 4(a)]. For a small pipette-sample distance, the particle traverses the areas of high current density next to the inner edges of the pipette tip opening. This results in a ring-shaped maximum in the image [Fig. 4(b)]. A low particle in the case of a large pipette-sample distance is imaged with a small height [Fig. 4(c)], because the current density is small far below the opening

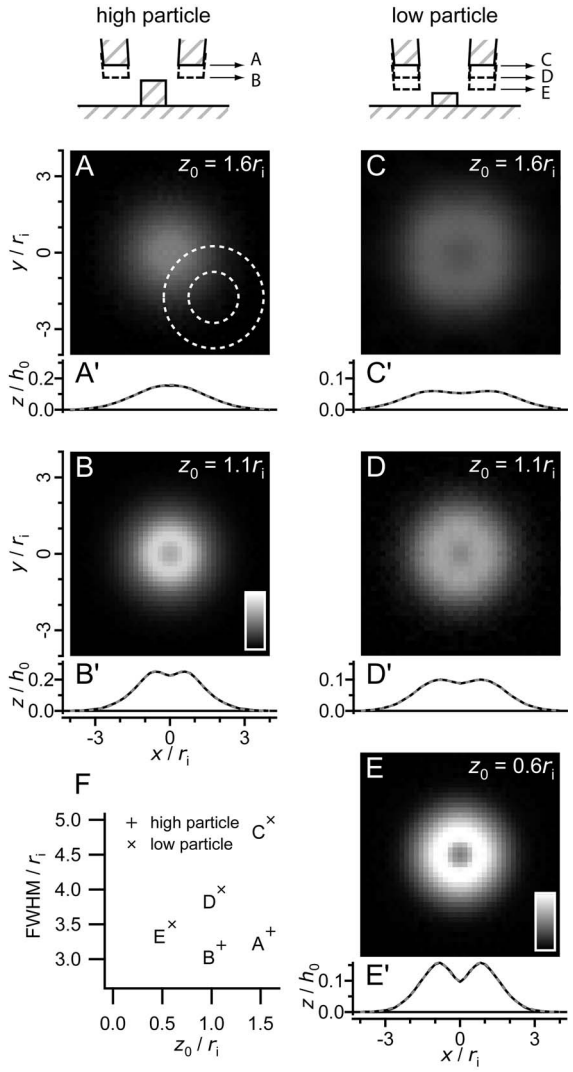

FIG. 4. Calculated topography images of a single cylindrical particle of radius $r=r_i/2$ on a planar surface. (a) A high particle, $h_0=r_i$, imaged at a large pipette-sample distance, $z_0=1.6r_i$, appears blurred in the image. The corresponding cross section (a') is bell-shaped with a height of $0.16h_0$ and a FWHM of $3.2r_i$. [(b) and (b')] Decreasing the pipette-sample distance, $z_0=1.1r_i$, causes an increase in the apparent height and a dip to appear in the center. [(c) and (c')] A low particle, $h_0=r_i/2$, results in an overproportionally smaller apparent height and is always imaged as a ring, both at a large pipette-sample distance, $z_0=1.6r_i$, and at smaller pipette-sample distances, [(d) and (d')] $z_0=1.1r_i$ and [(e) and (e')] $z_0=0.6r_i$. The color bars indicate height ranges of 0.0–$0.32h_0$ [(a) and (b)] and 0.0–$0.16h_0$ [(c)–(e)], respectively. The pipette tip opening with inner radius r_i and outer radius $r_o=2r_i$ is outlined as dashed circles in (a). (f) FWHM values as a function of pipette-sample distance, z_0, for the high and low particles, respectively. The FWHM decreases with the pipette-sample distance to a minimum value of about $3.0r_i$.

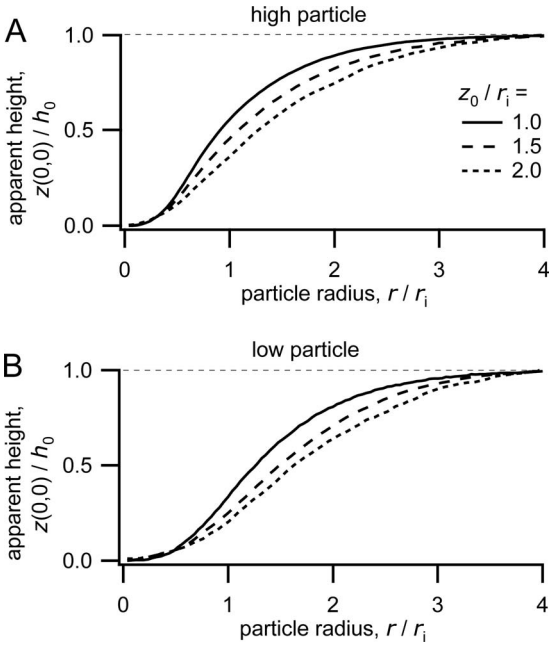

FIG. 5. Calculated apparent height of a single cylindrical particle on a planar surface in a SICM image, as a function of particle radius r. Actual particle heights (a) $h_0=r_i$ and (b) $h_0=r_i/2$. For $r\geq 3r_i$ the apparent height closely matches the actual height. For $r<3r_i$ the apparent height is significantly decreased and becomes zero for $r=0$. The different traces represent different pipette-sample distances z_0.

[Fig. 2(b)]. In such a case the experimenter would generally decrease the pipette-sample distance to increase the magnitude of the current density below the opening, in order to obtain more topographic contrast [Fig. 4(d)]. The low particle appears ring-shaped in both cases due to the ring-shaped distribution of the current density close to the sample [Fig. 2(c)]. We note that this effect causes small dips or pores in the sample to be imaged as ring-shaped valleys. For an even smaller pipette-sample distance the "squeezing" of the current directly below the pipette walls [Fig. 2(d)] becomes even more apparent. This enhances the ring-shaped appearance of the particle even more [Fig. 4(e)].

D. Apparent height of small particles

To further quantify the accuracy of height measurements in SICM we calculated the apparent height of a high cylindrical particle ($h_0=r_i$) at its center as a function of its radius [Fig. 5(a)]. For a large particle radius ($r\geq 3r_i$), the apparent height closely matches the actual physical height. For a decreasing radius ($r<3r_i$), the apparent height decreases, reaching zero at $r=0$. The larger the pipette-sample distance z_0 is, the earlier the height decreases [calculations for three different values of z_0 are shown as different traces in Fig. 5].

To assess the influence of the actual particle height h_0 on the apparent particle height, we repeated the calculations for a low particle [$h_0=r_i/2$, Fig. 5(b)]. A similar behavior as before is observed, but the apparent height starts decreasing at even larger particle radii. We note that in Fig. 5 we plotted the apparent height of the particle at its center. This means that in the case that a dip is developed in the particle image this height is somewhat lower than the maximum image height. But we also note that a dip can be developed only for small particle radii ($r<\approx r_i$).

In general, we find that objects with a lateral width below $\approx 6r_i$ are imaged with an apparent height that is a fraction of the actual height.

E. Two particles on a planar surface

In order to quantify the lateral resolution of SICM imaging we now consider two identical particles, spaced apart by a distance d [Figs. 6(a)–6(d)]. As before in the case of the single particle, we calculate topography images of these particles. We chose a large pipette-sample distance for the high particles and a small pipette-sample distance for the low particles since this choice represents optimal experimental conditions.

Figures 6(e)–6(h) show images of two high particles ($h_0=r_i$) imaged with a large pipette-sample distance ($z_0=1.6r_i$). At a large particle distance [Fig. 6(e), $d=6r_i$], the particles are clearly separated in the image, each appearing with a bell-shaped profile along the line through the centers of the particles [Fig. 6(e)', black trace]. This profile is reproduced by adding the height profiles of two individual particles as calculated in Fig. 4(a)' [Fig. 6(e)', gray dashed trace]. This fact will be used in Sec. III G to justify the use of a special point spread function (sPSF). When the particle distance is reduced [Figs. 6(f) and 6(g)], the particles start to overlap in the image, finally appearing as one single particle [Fig. 6(h)]. This overlapping behavior can also be observed in the corresponding cross sections [Figs. 6(f)' and 6(g)']. For very close particles the cross section [Fig. 6(h)'] again appears with a bell-shaped profile of the same width but twice the height ($0.30h_0$) as compared to a single particle image.

Figures 6(i)–6(l) show images of two low particles ($h_0=r_i/2$) at a small pipette-sample distance ($z_0=0.6r_i$). For a large particle distance [Fig. 6(i), $d=6r_i$] each particle is imaged as a single ring, corresponding to Fig. 4(e). The radius of each ring is about the inner pipette tip opening radius, r_i. Reducing the particle distance causes the rings to overlap [Fig. 6(j), $d=4r_i$]. When the particles are even closer [Fig. 6(k), $d=2r_i$], the overlap region appears with twice the apparent height of a single particle [$0.30h_0$ instead of $0.16h_0$ in Figs. 4(e) and 6(i)]. Finally, for a very small particle distance [Fig. 6(l), $d=r_i$] the resulting image exhibits two peaks, one above and one below the center between the particles. This is because the rings now overlap most strongly away from the x-axis. Two low particles, close to each other, therefore appear with two maxima, whose lateral orientation is rotated by 90°. Care must be taken to not interpret such an image as two particles oriented in y-direction.

F. Lateral resolution

To motivate a definition of "lateral resolution," we display cross sections through topography images of two particles at varying distance, d, as a grayscale plot [Fig. 7(a)]. For a large particle distance [left hand side in Fig. 7(a)] the particles are imaged as two separated bell shapes [corre-

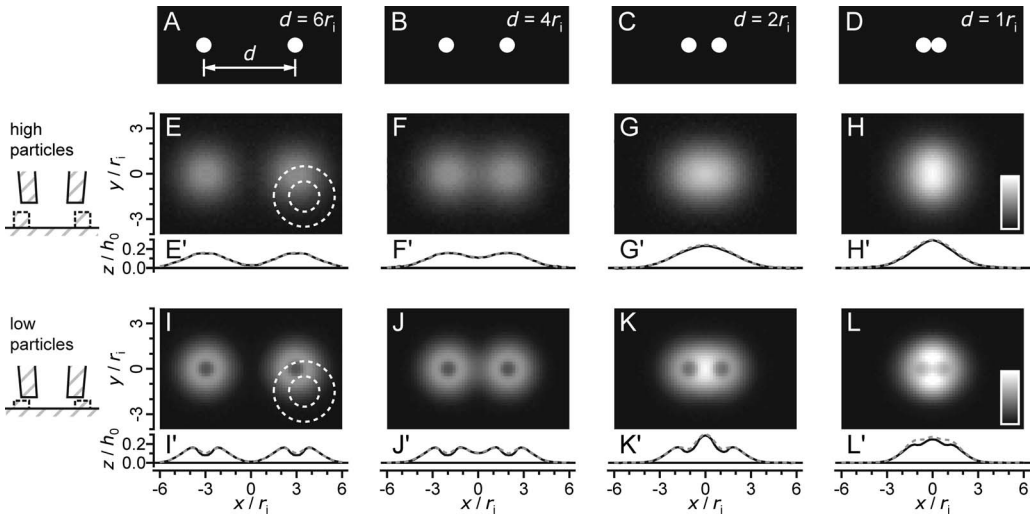

FIG. 6. Calculated topography images of two cylindrical particles of radius $r=r_i/2$ on a planar surface. [(a)–(d)] Actual topography. [(e)–(h)] Calculated topography images for two high particles, $h_0=r_i$, and a large pipette-sample distance, $z_0=1.6r_i$. [(i)–(l)] Images for low particles, $h_0=r_i/2$, and a small pipette-sample distance, $z_0=0.6r_i$. (e) At a large particle distance, $d=6r_i$, each high particle is imaged as a single bell shape [black trace in cross section (e')]. This is equivalent to the superposition of two single particle images from Fig. 4(a) [gray dashed trace in (e')]. [(f) and (f')] For a decreasing distance, $d=4r_i$, the bell shapes start to overlap and are not resolvable from each other any more for [(g) and (g')] $d=2r_i$ and [(h) and (h')] $d=r_i$. (i) At a large particle distance, $d=6r_i$, each low particle images as a ring [black trace in cross section (i')]. This is equivalent to the superposition of two single particle images from Fig. 4(e) [gray dashed trace in (i')]. [(j) and (j')] The rings start to overlap for $d=4r_i$. [(k) and (k')] For a smaller particle distance the rings overlap in the center between the particles. [(l) and (l')] For an even smaller distance the largest overlap is above and below the x-axis. In this case, the image appears as if two particles rotated by 90° were present. The color bars indicate a height range of $0.0-0.3h_0$. The pipette tip opening is outlined dashed in (e) and (i).

sponding to Figs. 6(e) and 6(f)]. For a small particle distance [right hand side in Fig. 7(a)] the particles appear as a single bell shape [corresponding to Figs. 6(g) and 6(h)]. We now plot the apparent height of the particles at the positions of their centers, $z(\pm d/2,0)$, and at the position centrally between the particles, $z(0,0)$ [Fig. 7(b), solid and dashed traces, respectively]. For a large particle distance, the apparent height of the individual particles is constant [solid trace, left hand side in Fig. 7(b)], and the apparent height at the position centrally between them is zero [dashed trace, left hand side in Fig. 7(b)]. This makes the particles clearly resolvable from each other. For a decreasing particle distance, the depth of the dip between the particles decreases (the solid and dotted traces approach each other). At $d=3r_i$ [black arrow in Fig. 7(b)], the two traces cross and the dip between the particles vanishes. At this point, the two particles cannot clearly be resolved from each other any more. We therefore define the lateral resolution of the SICM as the distance where $z(0,0)/z(\pm d/2,0)=1$. This distance is reached at $d_0=3r_i$. Such a definition of lateral resolution agrees with the value of FWHM in an image of a single particle (Fig. 4). The FWHM decreases for a decreasing pipette-sample distance z_0, but a minimum FWHM (for $z_0\rightarrow 0$) can be estimated as $\approx 3r_i$.

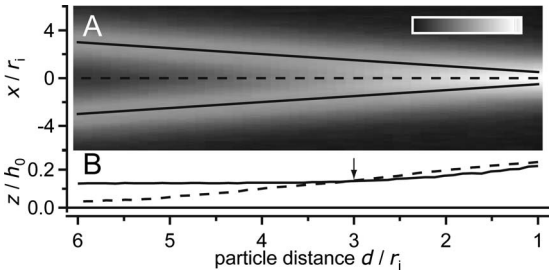

FIG. 7. (a) Topography image profile of two cylindrical particles at varying distance. The grayscale plot is constructed by cross sections through the particles [vertical axis; equivalent to Fig. 5(e)' to Fig. 5(h)'] while decreasing the particle distance d (horizontal axis). At sufficiently large particle distances, $d>3r_i$, a minimum is present between the particles, allowing to clearly resolve them from each other. For $d\leq 3r_i$ the particles are imaged as a single peak and cannot be resolved from each other. The color bar indicates a height range of $0.0-0.25h_0$. (b) Image height at the positions of the particles (continuous trace) and between them (dashed trace). The lateral resolution is defined as the distance at which the dip between the particles vanishes, i.e., where the continuous and the dashed traces cross. This corresponds to a distance three times the inner radius of the pipette tip opening, $d_0=3r_i$ (black arrow).

We note that care has to be taken when assessing resolution via the apparent width of a small object,[16] because such an object can artificially be made to appear arbitrarily narrow, depending on threshold conditions applied.

We also note that the lateral resolution d_0 varies slightly with changing pipette-sample distance and pipette wall thickness. Furthermore, a complementary imaging technique such as shear force imaging[8] could be used to achieve a higher topographic resolution while simultaneously recording the local ion current with SICM.

G. Contrast transfer function

Lateral resolution can alternatively be assessed by the contrast transfer function (CTF) of the microscope.[17] The CTF describes the sign and the magnitude of the microscope's response as a function of spatial frequency $f=1/r$. This method has successfully been applied to optical and electron microscopies, and also to scanning probe microscopy, such as magnetic force microscopy[18,19] and piezoresponse force microscopy.[20] A CTF can be defined if the imaging process of the microscope can be described by linear system theory, i.e., if a characteristic point spread function

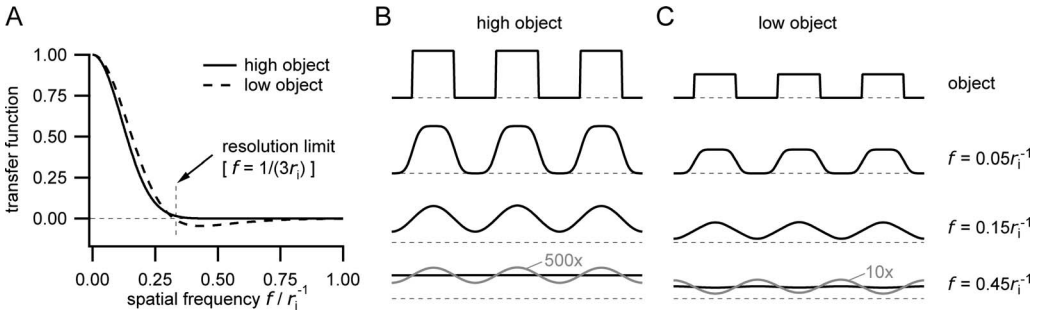

FIG. 8. (a) sCTF of the microscope as a function of spatial frequency f for a high object and a large pipette-sample distance ($h_0=r_i$ and $z_0=1.6r_i$, solid trace) and for a low object and a small pipette-sample distance ($h_0=r_i/2$ and $z_0=0.6r_i$, dashed trace). The sCTF is unity at small frequencies (wide objects), decreases for increasing frequencies (narrower objects), and becomes approximately zero above the resolution limit [$f>1/(3r_i)$]. [(b) and (c)] Calculated image profiles of a periodic array of rectangular stripes representing (b) a high object and (c) a low object for three different spatial frequencies. For increasing frequencies (upper to lower traces) the image profiles become smeared out and the apparent height of the stripes decreases. For high frequencies above the resolution limit (lower traces, gray traces show profiles with vertical scaling factors of 500 and 10, respectively) the apparent height approaches zero. Additionally, the profile is inverted in the case of a low object and small pipette-sample distance.

(PSF) exists.[21–23] In the case of SICM this is generally not fulfilled, because different pipette-sample distances and object heights cause the objects being imaged differently (as described previously in Sec. III C and shown in Fig. 4). However, for a given pipette-sample distance, z_0, and a given object height, h_0, we empirically found that the imaging process can be approximated by the convolution with a special PSF (sPSF), which is proportional to the image of a pointlike particle such as in Fig. 4. Empirically, we found a good functional approximation of the sPSF as

$$\mathrm{sPSF}(r) = A\,\exp(-r^2/a^2) - B\,\exp(-r^2/b^2). \tag{4}$$

For example, for a high object ($h_0=r_i$) imaged at a large pipette-sample distance ($z_0=1.6r_i$) [Fig. 4(a)], the parameters are $A=0.084r_i^{-2}$, $a=1.95r_i$, and $B=0$ [obtained by fitting Eq. (4) to the image in Fig. 4(a) and normalization]. For a low object ($h_0=r_i/2$) imaged at a small pipette-sample distance ($z_0=0.6r_i$) [Fig. 4(e)] the parameters are $A=0.148r_i^{-2}$, $a=1.57r_i$, $B=0.092r_i^{-2}$, and $b=0.72r_i$. The respective sPSFs are plotted as gray dashed traces in Fig. 4(a)' to Fig. 4(e)'. To justify the assumption of a linear imaging system we used convolution with the sPSFs obtained here to construct image profiles of the two particles [gray dashed traces in Fig. 6(e)' to Fig. 6(l)']. These profiles match the respective FEM results [solid lines in Fig. 6(e)' to Fig. 6(l)'] reasonably well.

The special CTF (sCTF) is given by the Fourier transform of the sPSF[24]

$$\mathrm{sCTF}(f) = \pi A a^2\,\exp(-\pi^2 f^2 a^2) - \pi B b^2\,\exp(-\pi^2 f^2 b^2), \tag{5}$$

and is shown in Fig. 8(a) for the two special cases considered here. In both cases, the sCTF is centered at spatial frequency $f=0$, is unity at small frequencies (wide objects), and approaches zero at large frequencies (narrow objects). For the high object and the large pipette-sample distance the sCTF is Gaussian-shaped. For the low object and the small pipette-sample distance the sCTF becomes negative for $f\geq 0.32r_i^{-1}$.

To illustrate the influence of the shape of the sCTF on the imaging process Figs. 8(b) and 8(c) show the image profiles of a periodic array of rectangular stripes as an object (top traces) with a fundamental spatial frequency f, constructed by convolution with the respective sPSF. First we consider the high object and the large pipette-sample distance [Fig. 8(b)]. In the case of a low frequency ($f=0.05r_i^{-1}$, upper trace) the object's height is imaged correctly, even though its edges are smeared out because the objects' higher harmonics are damped by the sCTF. For an increasing frequency ($f=0.15r_i^{-1}$, middle trace) the height in the image is reduced (due to the decreasing sCTF) and becomes sinusoidal. For an even higher frequency ($f=0.45r_i^{-1}$, lower trace, gray trace shown with a vertical scaling factor of 500) the image height approaches zero, corresponding to the vanishing value of the sCTF. For the low object and the small pipette-sample distance [Fig. 8(c)] the imaging process is similar, except at high frequencies ($f=0.45r_i^{-1}$, lower trace, gray trace shown with a vertical scaling factor of 10), where the negative sign of the sCTF causes the object to appear inverted.

Nonmonotonic sections and sign reversals in the CTF should generally be avoided due to resulting image artifacts [e.g., the "ring artifact" in Figs. 6(i)–6(l)]. In optical and electron microscopies this is done by defining the "Scherzer resolution,"[24,25] which is the frequency where the CTF crosses zero for the first time. This alternative definition of lateral resolution is similar but slightly more conservative compared to our result obtained in Sec. III F. In our definition of resolution in real space, $d_0=3r_i$, corresponding to $f=1/(3r_i)=0.33r_i^{-1}$ in frequency space, the sCTF has decreased significantly.

We note that care needs to be taken when estimating the lateral resolution in frequency space, because spatial frequencies above the lateral resolution limit [see Fig. 8(a)] can be observed in some cases (limited only by instrumental noise) due to the asymptotic behavior of the sCTF, and can be enhanced with postprocessing methods. This especially applies to samples with correlated features such as periodic samples, as demonstrated in Figs. 8(b) and 8(c). By using correlation averaging, for example, features smaller than the lateral resolution $d_0=3r_i$ as defined in Sec. III F may be resolved on a periodic sample.[3] However, one needs to con-

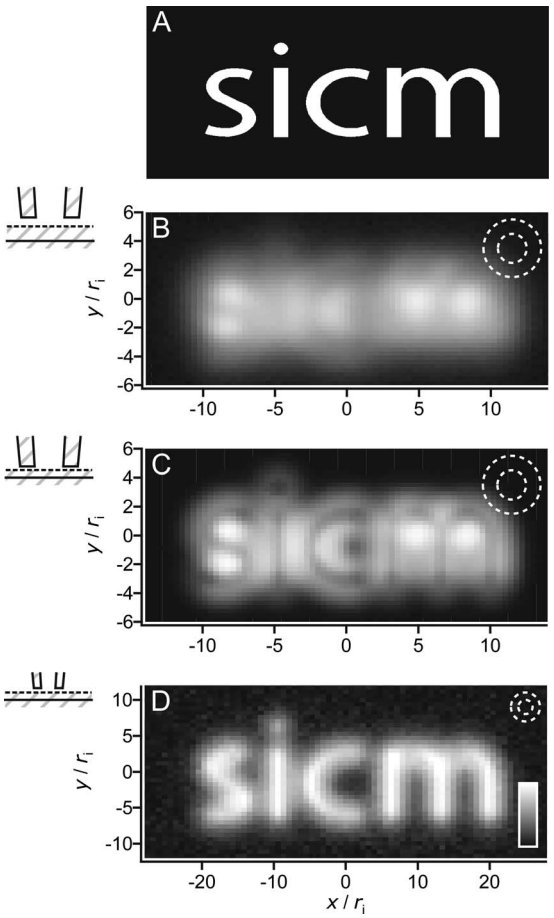

FIG. 9. Calculated topography images of a "sicm-shaped" object. (a) Actual topography. (b) Topography image of a high object, $h_0=r_i$, imaged with a large pipette at a large pipette-sample distance, $z_0=1.6r_i$. (c) Topography image of a low object, $h_0=r_i/2$, imaged with a large pipette at a small pipette-sample distance, $z_0=0.6r_i$. (d) Topography image of the same object, imaged with a pipette half the size, at a corresponding large pipette-sample distance, $z_0=1.6r_i$. The letters are now clearly resolvable. The color bar indicates a height range of $0.0-0.8h_0$. The cross sections of the respective pipette tip openings are outlined dashed in the images.

sider that the resulting image is convoluted with the microscope's sPSF, so these features might as well be caused by the pipette tip.

In summary, we showed that individual features such as single defects or two closely spaced single particles can directly be identified with a lateral resolution of $d_0=3r_i$, even if higher frequency components are present in the image.

H. Imaging of a more complex object

In order to demonstrate the imaging of a more complex object we constructed an object shaped like the letters "sicm," with a constant height h_0 [Fig. 9(a)]. For a high object, $h_0=r_i$, imaged at a large pipette-sample distance, $z_0=1.6r_i$, the topography image is strongly blurred [Fig. 9(b)]. For a low object, $h_0=r_i/2$, imaged at a small pipette-sample distance, $z_0=0.6r_i$, the topography image exhibits ring artifacts [Fig. 9(c)]: Every linelike feature is imaged as two lines (e.g., the letters "i" and "c") and round shapes similar in curvature to the pipette tip opening appear especially large at the center of curvature ("s" and "m"). This results in dips appearing at the positions of the letters. If the size of the pipette is reduced by a factor of 2 the resulting image is still blurred but the letters are clearly resolvable [Fig. 9(d)].

IV. CONCLUSION

In this paper, we evaluated the process of image formation in SICM. First, we calculated the dependence of the ion current through the pipette as a function of pipette-sample distance by using FEM. This allowed correlating the experimentally set current drop value during topographic imaging to the resulting pipette-sample distance, which is not directly accessible from the experiment. In order to show the effect of pipette-sample distance and object height on image formation, we calculated topographic images of small particles. Particles with a large height, imaged at a large pipette-sample distance, appear with a bell-shaped profile. Particles with a small height or that are imaged at a small pipette-sample distance appear as rings. Small particles that are close to each other can appear with a lateral orientation that is rotated by 90°.

We found that objects with a lateral width below $\approx 6r_i$ are imaged with an apparent height that is a fraction of the actual height. The apparent height depends on several geometrical parameters. In the case that these parameters are known, our results can be used to reconstruct, in principle, the actual height.

We defined the lateral resolution in SICM as the distance at which two individual particles can just be separated in the image. We found that the lateral resolution is three times the inner opening radius of the pipette, $d_0=3r_i$, for the tip geometry considered here. We also showed that this definition sets a limit below which imaging artifacts can occur. We note that for a tilted or rough tip opening the resolution will generally be lower. However, no large changes are expected at large pipette-sample distances ($z_0 > \approx r_i$).

Finally, we note that the definition of lateral resolution is somehow arbitrary. However, our definition is both reasonable and useful, because it allows directly interpreting SICM images.

ACKNOWLEDGMENTS

We thank Matthias Böcker, Steffen Muschter, and Yuri Korchev for stimulating discussions. We acknowledge financial support from the DFG (Grant No. SCHA 1264/1-2) and from the Gemeinnützige Hertiestiftung/Stifterverband für die Deutsche Wissenschaft.

[1] P. K. Hansma, B. Drake, O. Marti, S. A. Gould, and C. B. Prater, Science **243**, 641 (1989).
[2] Y. E. Korchev, C. L. Bashford, M. Milovanovic, I. Vodyanoy, and M. J. Lab, Biophys. J. **73**, 653 (1997).
[3] A. I. Shevchuk, G. I. Frolenkov, D. Sanchez, P. S. James, N. Freedman, M. J. Lab, R. Jones, D. Klenerman, and Y. E. Korchev, Angew. Chem., Int. Ed. Engl. **45**, 2212 (2006).
[4] J. Gorelik, A. I. Shevchuk, G. I. Frolenkov, I. A. Diakonov, M. J. Lab, C. J. Kros, G. P. Richardson, I. Vodyanoy, C. R. Edwards, D. Klenerman, and Y. E. Korchev, Proc. Natl. Acad. Sci. U.S.A. **100**, 5819 (2003).
[5] J. Gorelik, Y. Zhang, D. Sánchez, A. I. Shevchuk, G. I. Frolenkov, M. J. Lab, D. Klenerman, C. Edwards, and Y. E. Korchev, Proc. Natl. Acad. Sci. U.S.A. **102**, 15000 (2005).
[6] M. Böcker, S. Muschter, E. K. Schmitt, C. Steinem, and T. E. Schäffer, Langmuir **25**, 3022 (2009).

[7]A. Bruckbauer, L. M. Ying, A. M. Rothery, Y. E. Korchev, and D. Klenerman, Anal. Chem. **74**, 2612 (2002).
[8]M. Böcker, B. Anczykowski, J. Wegener, and T. E. Schäffer, Nanotechnology **18**, 145505 (2007).
[9]D. Sánchez, N. Johnson, C. Li, P. Novak, J. Rheinlaender, Y. Zhang, U. Anand, A. Praveen, J. Gorelik, G. Frolenkov, C. Benham, M. Lab, V. Ostanin, T. E. Schäffer, D. Klenerman, and Y. Korchev, Biophys. J. **95**, 3017 (2008).
[10]H. Nitz, J. Kamp, and H. Fuchs, Probe Microsc. **1**, 187 (1998).
[11]O. A. Adenle and D. G. Fitzgerald, Conf. Proc. IEEE Eng. Med. Biol. Soc. **4**, 3410 (2005).
[12]T. K. Chowdhury, J. Phys. E **2**, 1087 (1969).
[13]K. T. Brown and D. G. Flaming, *Advanced Micropipette Techniques for Cell Physiology* (Wiley, New York, 1986).
[14]A. I. Shevchuk, J. Gorelik, S. E. Harding, M. J. Lab, D. Klenerman, and Y. E. Korchev, Biophys. J. **81**, 1759 (2001).
[15]D. Pastré, H. Iwamoto, J. Liu, G. Szabo, and Z. Shao, Ultramicroscopy **90**, 13 (2001).
[16]P. Novak, C. Li, A. I. Shevshuk, R. Stepanyan, M. Caldwell, S. Hughes, T. G. Smart, J. Gorelik, V. P. Ostanin, M. J. Lab, G. W. J. Moss, G. I. Frolenkov, D. Klenerman, and Y. E. Korchev, Nat. Methods **6**, 279 (2009).
[17]O. Scherzer, J. Appl. Phys. **20**, 20 (1949).
[18]P. J. A. van Schendel, H. J. Hug, B. Stiefel, S. Martin, and H.-J. Güntherodt, J. Appl. Phys. **88**, 435 (2000).
[19]H. J. Hug, B. Stiefel, P. J. A. van Schendel, A. Moser, R. Hofer, S. Martin, H. J. Güntherodt, S. Porthun, L. Abelmann, J. C. Lodder, G. Bochi, and R. C. O'Handley, J. Appl. Phys. **83**, 5609 (1998).
[20]S. V. Kalinin, S. Jesse, B. J. Rodriguez, J. Shin, A. P. Baddorf, H. N. Lee, A. Borisevich, and S. J. Pennycook, Nanotechnology **17**, 3400 (2006).
[21]J. C. Dainty and R. Shaw, *Image Science*, 1st ed. (Academic, London, 1974).
[22]J. D. Gaskill, *Linear Systems, Fourier Transforms, and Optics*, 1st ed. (Wiley, Malden, MA, 1978).
[23]J. W. Goodman, *Introduction to Fourier Optics*, 3rd ed. (Roberts & Company, Greenwood Village, CO, 2004).
[24]O. Sherzer, J. Appl. Phys. **20**, 20 (1949).
[25]M. A. O'Keefe, Ultramicroscopy **47**, 282 (1992).